Phase-Specific Vapor-Liquid-Solid Growth of GeSe and $GeSe_2$ Van der Waals Nanoribbons and Formation of GeSe-$GeSe_2$ Heterostructures

Eli Sutter,[1,2,*] Jacob S. French,[3] and Peter Sutter[3]

[1]*Department of Mechanical and Materials Engineering, University of Nebraska-Lincoln, Lincoln, NE 68588 (USA)*
[2]*Nebraska Center for Materials and Nanoscience, University of Nebraska-Lincoln, Lincoln, NE 68588 (USA)*
[3]*Department of Electrical and Computer Engineering, University of Nebraska-Lincoln, Lincoln, NE 68588 (USA)*

ABSTRACT

Group IV (Ge, Sn) chalcogenides differ from most other 2D/layered semiconductors in their ability to crystallize both as stable mono- and dichalcogenides. The associated diversity in structure and properties presents the challenge of identifying conditions for the selective growth of the different crystalline phases, as well as opportunities for phase conversion and materials integration/interface formation in heterostructures. Here, we discuss the phase-selective synthesis of free-standing GeSe and $GeSe_2$ nanoribbons in a vapor-liquid-solid growth process over Au catalyst nanoparticles. Electron microscopy shows that the two types of ribbons adopt high-quality van der Waals structures with layering in the ribbon plane and with the ribbon axis aligned with the ***b***-axis of GeSe and $GeSe_2$, respectively. Non-specific growth gives rise to a tapered morphology, and in the case of $GeSe_2$ leads to nucleation of misoriented crystallites on the ribbon surface. The partial transformation of GeSe ribbons by selenization, finally, reacts the outermost layers and edges to $GeSe_2$, thus producing GeSe-$GeSe_2$ core-shell heterostructures. Cathodoluminescence spectroscopy of as-grown GeSe ribbons and of GeSe-$GeSe_2$ hybrids shows a marked enhancement of the luminescence intensity due to surface passivation by wide-bandgap $GeSe_2$ (E_g = 2.5 eV). Our results support applications of germanium mono- and dichalcogenides as well as their heterostructures in areas such as optoelectronics and photovoltaics.

*Corresponding author: esutter@unl.edu

INTRODUCTION

Group IV chalcogenides can crystallize both as layered monochalcogenides (MX, where M = Ge, Sn; X = S, Se) as well as dichalcogenides (MX_2). The existence of multiple stable layered phases with different stoichiometry distinguishes these materials from most other 2D/layered semiconductors. The group IV monochalcogenides generally crystallize with anisotropic orthorhombic layered structures (GeSe,[1-2] GeS,[3-4] SnS,[3,5] *etc.*) analogous to black phosphorous, while the dichalcogenides exhibit various 2D layered (trigonal for SnS_2 and $SnSe_2$;[6] monoclinic for $GeSe_2$,[7] *etc.*) and occasionally 3D-crystalline structures. The existence of mono- and dichalcogenide phases permits *(i)* phase engineering during growth to obtain either of the two stable phases; *(ii)* a facile conversion between the two phases, controlled *via* the chalcogen chemical potential, μ_X (which, in turn, is governed by experimental parameters such as the vapor pressure of the chalcogen species); and *(iii)* the integration of mono- and dichalcogenides in hybrids or heterostructures. Phase-engineered growth, interconversion, and integration have been demonstrated for the SnS-SnS_2 system. During growth from SnO_2 and S, the product phase can be selected *via* the substrate temperature, with low temperatures favoring SnS_2 whereas SnS is obtained at high temperatures.[8] Electron-stimulated formation of sulfur vacancies in vacuum (*i.e.*, at low μ_S) can convert SnS_2 into crystalline SnS,[9-10] while the supply of excess S can controllably transform ultrathin SnS into SnS_2.[11] The integration of SnS and SnS_2 has yielded wrap-around heterostructures that show extended long-wavelength light harvesting *via* spatially indirect interfacial absorption reaching into the short-wavelength infrared.[12]

The phase-selected growth of germanium mono- and diselenides is desirable to access the different properties of these chalcogenides. In addition, the integration of GeSe and $GeSe_2$ may offer emergent functionalities by combining layered semiconductors with different structure and

electronic properties. Germanium selenide (GeSe) has attracted interest for its highly anisotropic properties such as absorbance and polarization-dependent photoresponse,[13-16] and ferroelectric behavior[17] due to the anisotropic structure of the layers. GeSe has a direct bandgap of 1.3 eV,[18] which makes it suitable for optoelectronic applications, such as near-infrared photodetection and as a p-type absorber material for photovoltaics. Polycrystalline GeSe films have been incorporated in solar cells with power conversion efficiency up to 5.2%.[19-20] While germanium diselenide ($GeSe_2$) can crystallize in two different polymorphs, nanostructures such as flakes[21-22] and nanobelts[23-26] invariably crystallize in the layered monoclinic β-$GeSe_2$ structure.[21-22,27-29] $GeSe_2$ has a significantly larger bandgap than GeSe, reported to be between 2.25 eV[30] – 2.7 eV[21,29] at room temperature. $GeSe_2$ may thus be considered as a possible candidate for replacing the conventional wide-bandgap CdS window layer when paired with GeSe in an all-$GeSe_x$ solar cell architecture. CVD from halide (GeI_2) and Se precursors has shown control over the phase of the resulting flakes (GeSe *vs.* $GeSe_2$) on different substrates.[22]

Here we demonstrate the phase-controlled synthesis of GeSe and $GeSe_2$ ribbons by a vapor-liquid-solid (VLS) process over Au catalyst nanoparticles. Transmission electron microscopy (TEM) shows that the synthesized ribbons are single-crystalline and crystallize in the layered orthorhombic GeSe (space group Pnma) and monoclinic β-$GeSe_2$ structure (space group $P2_1/c$), respectively. TEM imaging of the nanoribbons is used to deduce their growth pathway. We then discuss a simple route toward the formation of GeSe-$GeSe_2$ heterostructures by solid-state selenization of GeSe ribbons in selenium vapor at near-ambient pressures and at different temperatures. We establish suitable conditions for the conversion of the outermost layers of the GeSe ribbons to layered β-$GeSe_2$. Nanoscale cathodoluminescence measurements demonstrate the efficient surface passivation of GeSe by $GeSe_2$, which results in an enhanced radiative

recombination and luminescence of GeSe at room temperature. The simple passivation strategy lends itself to incorporation in GeSe optoelectronic devices and photovoltaic cells, where it can help reduce non-radiative recombination.

RESULTS AND DISCUSSION

Phase-controlled vapor-liquid-solid (VLS) growth of germanium selenide nanoribbons was carried out in a two-zone tube furnace by vapor transport of the precursors on Si(100) substrates covered by thin (2-5 nm) Au films, which dewetted into polydisperse Au particle VLS catalysts at the growth temperature (see Methods for details). Growth from a pure GeSe precursor (evaporated as an intact formula unit) at substrate temperatures between 280–340°C resulted in forests of GeSe nanoribbons,[2] with individual ribbons shown in Fig. 1(a). Switching the product to $GeSe_2$ ribbons requires two changes to the growth process: *(i)* Addition of selenium to the vapor-phase precursor by thermal evaporation from a separate crucible with molten Se; and *(ii)* an increase of the substrate temperature to 400°C. Using these conditions, we find that the growth substrates are covered with a new type of 1D nanostructure, identified below as ribbons of monoclinic □-$GeSe_2$.

A detailed characterization of the GeSe ribbons obtained by VLS growth from a pure GeSe precursor at lower substrate temperatures has been reported previously,[2] showing them to be GeSe single-crystals (Fig. 1 (b), (c)) with layering in the ribbon plane and symmetry axis aligned along the GeSe ***b***-axis. Here, we focus on the analysis of the ribbons obtained from GeSe and Se vapors at higher temperature. Optical images show that the ribbons grow dense on the Au/Si substrate (Fig. S1 (a)). Raman spectra of the ensemble of the nanostructures on the growth substrate (Fig. S1 (b)) show the characteristic Raman modes of monoclinic $GeSe_2$.[22] The structural investigation of individual 1D nanostructures was carried out by TEM (Fig. 1(e)-(h),

Fig. 2, Fig. S2). Individual 1D nanostructures with lengths exceeding 15 µm were observed after dry transfer to carbon TEM grids, suggesting that on the native support they grow up to several tens of µm in length (Fig. 1, Fig. 2). Their typical width is ~1 µm or below, and they usually appear strongly tapered, *i.e.*, their width increases from tip to base. At the tip, the

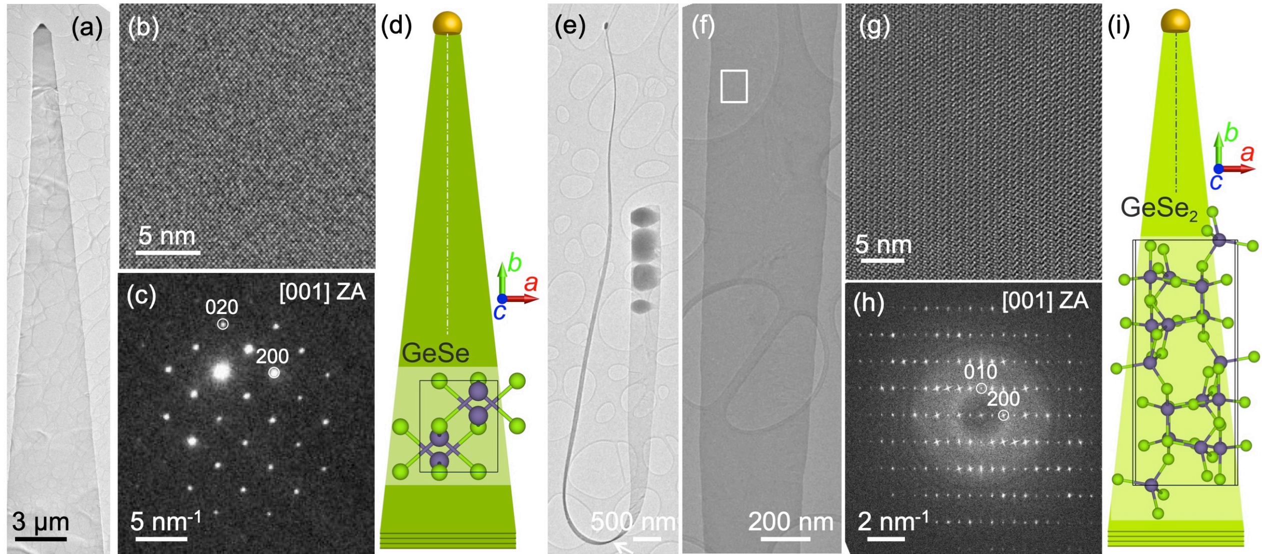

Figure 1. Phase-controlled VLS growth of $GeSe_x$ (x = 1, 2) nanoribbons. (a) – (d) GeSe ribbons from a pure GeSe precursor. (a) TEM image of a characteristic GeSe ribbon. **(b)** HRTEM image showing the orthorhombic GeSe lattice. **(c)** Selected-area electron diffraction pattern indexed to orthorhombic GeSe (*Pnma*) along [001] zone axis (ZA). **(d)** Schematic of the GeSe ribbon morphology overlayed with the GeSe atomic model: Basal-plane in the plane of the ribbon, ribbon axis along the GeSe ***b***-axis. **(e) – (h) $GeSe_2$ ribbons from mixed GeSe and Se precursors. (e)** TEM image of a characteristic $GeSe_2$ ribbon. **(f)** Higher magnification TEM image of the ribbon. **(g)** High-resolution TEM image of the area marked in (f) showing the monoclinic β-$GeSe_2$ lattice viewed along the [001] zone axis. **(h)** Fast-Fourier transform of the HRTEM image shown in (g), indexed to β-$GeSe_2$ (*$P2_1/c$*). **(i)** Schematic of the $GeSe_2$ ribbon morphology overlayed with the $GeSe_2$ atomic model: Basal-plane in the plane of the ribbon, ribbon axis along the $GeSe_2$ ***b***-axis.

1D nanostructures show a characteristic darker TEM contrast (Fig. 1 (a), (d), Fig. 2 (a)), consistent with the Au catalyst particle with higher average atomic number, *Z*. High-resolution (HR) TEM imaging and corresponding fast-Fourier transforms (FFT) (Fig. 1(g)-(h)) confirm that they are single crystalline nanoribbons consisting of layered $GeSe_2$ (monoclinic, $P2_1/c$, $\boldsymbol{a}$ = 17.25 Å, $\boldsymbol{b}$ = 7.20 Å, $\boldsymbol{c}$ = 12.89 Å, JCPDS No. 71-0117).[7] When viewed along the [001] zone axis, HRTEM imaging shows the characteristic atomic structure of the $GeSe_2$ basal plane (Fig. 1 (g)). Basal-plane imaging allows to easily determine the morphology and the symmetry axes of the

ribbons and confirms that the ***c***-axis (*i.e.*, the van der Waals stacking direction) is perpendicular to the ribbon plane, similar to the cases of GaS, GaSe, and GeSe nanoribbons reported earlier.[2,31-32] Fig. 1 (h) and Fig. S2 show that the symmetry axis (and primary growth direction) of the ribbons is oriented along the [010] crystallographic direction (*i.e.*, the $GeSe_2$ ***b***-axis).

The ribbons appear to easily twist during the transfer to the TEM support and frequently exhibit a vertical section that is viewed perpendicular to the basal plane (Fig. 1 (e), arrow; Fig. 2 (a), white rectangle). Due to the twisting, the ribbons transition continuously between horizontal segments (labeled 'h' in Fig. 2 (a), viewed along the [001] zone axis), going through a vertical section (labeled 'v' in Fig. 2 (a); shown in detail in Fig. 2(b)), where they stand on edge, *i.e.*, are viewed along the [100] zone axis (within the plane of the van der Waals layers). This allows us to determine that the thickness of the ribbons is ~20 nm (Fig. 1 (e), Fig. 2 (b)). Comparison of

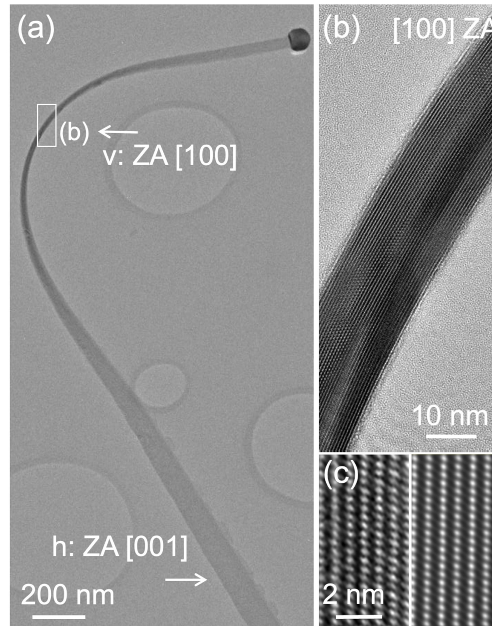

Figure 2. Thickness determination on twisted $GeSe_2$ nanoribbons. (a) TEM image of an axially twisted $GeSe_2$ nanoribbon that transitions continuously from planar to vertical and again to planar. **(b)** High-resolution TEM image obtained in the area marked in (a), where the ribbon is viewed along the [100] zone axis (ZA). **(c)** Higher magnification view of the $GeSe_2$ lattice fringes shown in (b) (left), and multi-slice TEM image simulation (right).

high-resolution TEM with multislice simulations further confirms these conclusions regarding the structure and local orientation in the vertical sections of the ribbons (Fig. 2 (c)).

Our TEM analysis demonstrates that the ribbons grown from GeSe and Se on Au/Si consist of single-crystalline layered □-$GeSe_2$ with layer stacking (***c***-axis) perpendicular to the ribbon axis, grown along the [010] direction (***b***-axis, Fig. 1 (i)). The presence of Au particles at the tips of the $GeSe_2$ ribbons suggests that the growth from GeSe and Se vapors proceeds *via* a VLS mechanism. Similar to the VLS growth of other van der Waals nanostructures, such as GeS nanowires,[33] GeSe,[2] and GaSe[31] nanoribbons, the combination of GeSe and Se precursors used here appears to combine with Au nanoparticles to form a (quasi)-binary eutectic, which acts as the active VLS catalyst in the growth of $GeSe_2$ ribbons. In a pure VLS growth the ribbons should maintain constant lateral dimensions defined by the size of the catalyst drop. However, the $GeSe_2$ ribbons increase in width from < 50 nm close to the tip to ~ 600-700 nm at a length of ~10 μm (Fig. 1 (e)). This observation confirms that the growth is a hybrid process, consisting of VLS catalyst mediated longitudinal growth accompanied by non-specific incorporation into the exposed edges of the ribbon. Similar hybrid growth has been observed for GeSe ribbons.[2] In the case of GeSe nanoribbon growth, however, the thickness is preserved, *i.e.*, secondary nucleation on top of the basal plane is suppressed.

TEM analysis shows a more complicated scenario for $GeSe_2$ ribbons. Close to the tips (*i.e.*, regions with shortest exposure times to the precursor vapors) the ribbons show uniform thickness but towards the base, TEM images reveal two types of deviation from the uniform contrast: *(i)* the central part retains uniform contrast, but towards one of the edges the ribbons become thinner. For instance, in Fig. S2 (b)-(e) it can be clearly seen that the left edge is straight while the right edge is stepped as the thickness of the ribbon decreases. *(ii)* All ribbons (Figs. 1 (a), 2) show

areas with much darker TEM contrast that can be associated with local thickening towards the base. This thickening – actually growth on top of the basal plane (Fig. 1 (e)) – appears anisotropic, adopting characteristic faceted rhombohedral shapes, similar to those found for $GeSe_2$ flakes on mica.[21] Fig. 3 (a) provides an opportunity for evaluating the extent of the growth on the basal plane of the ribbon. Similar to Fig. 2, the ribbon is twisted and the dashed line marks the transition from plane view (white arrow) close to the tip (Fig. 3 (b)) to edge view (red arrow). While the thickness of the ribbon itself is ~ 25 nm (Fig. 3 (c)), the thickness of the growth on top of it reaches ~125-130 nm. The additional growth is seen as bright contrast in high-angle annular dark field scanning TEM (HAADF-STEM) (Fig. 3 (d)).

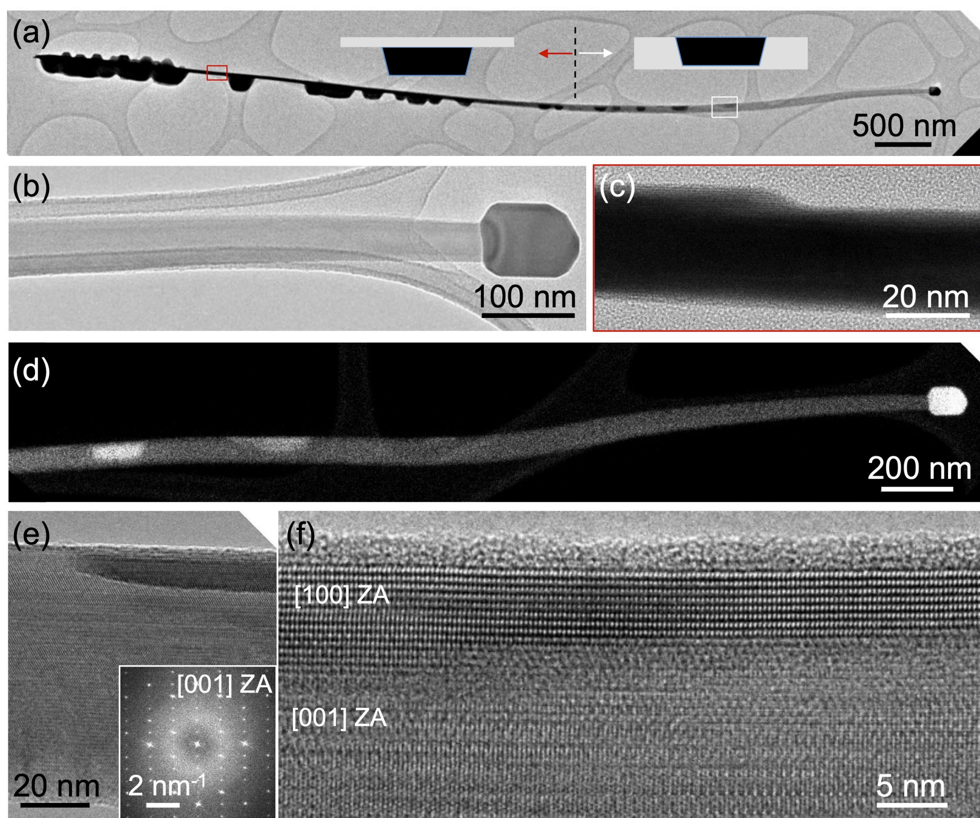

Figure 3. Non-specific growth on the basal plane of VLS $GeSe_2$ ribbons. (a) TEM image of an axially twisted $GeSe_2$ ribbon. The dashed vertical line marks the position at which the ribbons starts twisting, transitioning from plane view (right) to edge view (left). **(b)** Higher magnification TEM image of the planar ribbon section near the Au-rich tip, showing uniform contrast. **(c)** High-resolution TEM image of the area marked by a red rectangle in (a), where the ribbon is viewed edge-on. **(d)** HAADF-STEM image of the $GeSe_2$ ribbon showing areas with brighter contrast consistent with local thickening. **(e)** High-resolution TEM image of the area of the $GeSe_2$ ribbon marked by a white rectangle in (a), showing darker TEM

contrast due to thickening at the edge. Inset: Fast Fourier transform of the area of the $GeSe_2$ ribbon viewed close to the [001] zone axis. **(f)** Higher magnification view of the $GeSe_2$ lattice fringes at the thicker edge of the ribbon, viewed along the [100] zone axis (see also Fig. 2 (c)).

Thus, in $GeSe_2$ ribbons we find a combination of tapering, *i.e.*, lateral extension due to incorporation of material into the edges (Fig. 1 (e), Fig. 2), as well as additional growth on the basal plane of the ribbons. The latter is rather unusual in layered crystals, especially those with inert surfaces such as the chalcogen terminated transition metal dichalcogenides, where nucleation on the non-reactive basal plane is generally avoided. We can ascribe the additional growth observed here to the open structure of β-$GeSe_2$, which lacks an inert surface termination (see Fig. 1 (i)). The $GeSe_2$ material deposited on the basal plane of the ribbons is thicker towards the ribbon base, commensurate with the longer exposure to the vapor during growth (Fig. 3 (a)).[34] TEM imaging can shed light on the growth process, since images taken along the same ribbon are snapshots of the different stages of growth on the top facet. The very initial stages of nucleation and growth can be seen in the areas with darker contrast closer to the tip of the $GeSe_2$ ribbons (Fig. 3 (e)-(f)). HRTEM (Fig 3 (f)) shows that the nucleation occurs close to one edge of the ribbon, followed by the expansion of the nucleus toward the center and opposite edge with further growth. The added nuclei are not simply thicker, but they have a different crystallographic orientation than the rest of the ribbon. In the region shown in Fig. 3 (f), for example, the ribbon itself is viewed close to the [001] zone axis, while the thicker nucleus near the edge is viewed edge-on, *i.e.*, along the [100] zone axis. Further analysis shows that the added growth starts in a majority of ribbons at steps present at one of the edges (Fig. S2 (b), (d)), which provide preferred nucleation sites. Stepped edges are not unusual, for instance in GaSe ribbons the thickness can change significantly either at one or at both edges.[31] However, crystallographically misoriented 3D nucleation at such edges seems to be unique in $GeSe_2$ ribbons. Some of the ribbons lack stepped edges, *i.e.*, have uniform thickness throughout (Fig. 1

(e)). In such cases, extra growth on the top facet requires nucleation that is not facilitated by step sites. The resulting islands cover the entire ribbon width and assume faceted rhombic shapes.

In addition to phase-controlled growth, realized here *via* VLS processes under different growth conditions, the existence of stable group IV mono- and dichalcogenides provides opportunities for creating heterostructures between GeSe and $GeSe_2$. Similar heterostructures can be created spontaneously during growth[12,35-36] as well as during post growth processing.[37] Termination by chalcogen-rich, wide-bandgap $GeSe_2$ may provide an efficient electronic passivation at the surface, similar to sulfur-rich surface layers on Ge nanowires[38] and planar Ge surfaces.[39] Here we explore a strategy toward GeSe-$GeSe_2$ heterostructures involving the partial transformation of GeSe ribbons into the wider band gap $GeSe_2$ using selenization. GeSe ribbons were prepared by vapor transport of a GeSe precursor, as discussed above and shown in Fig. 1 (a)-(d).[2] However, to extend the temperature window for selenization we increased the temperature for the GeSe ribbon growth to 400°C, assuming that the ribbons are reasonably stable up to their growth temperature against decomposition by major GeSe loss. The morphology and stacking of the starting GeSe ribbons (prior to selenization) is shown in Fig. 4 (a)-(c). Similar to their counterparts grown at lower temperatures, the GeSe nanoribbons are orthorhombic layered single crystals. However, the ribbons grown at high temperature attain even larger sizes and their ends split into a characteristic comb-like morphology.[40] Furthermore, the higher growth temperature switches the edges from armchair to zigzag, *i.e.*, the ribbon axis now aligns along the GeSe ***a***-direction.

Solid-state selenization of the as-grown GeSe ribbons was carried out in a tube furnace with two temperature zones, using exposure to Se vapor in an Ar carrier gas at different temperatures (Fig. S3; see Methods). Comparison of the optical images of the GeSe ribbons before (Fig. S3

(b)), and after exposure to Se (Fig. S3 (d), (e)) show a pronounced change in contrast suggesting modifications in morphology that depend on the sample temperature during selenization. The TEM images in Fig. 4 (d)-(f) and Figs. S4-S6 show the morphology of representative GeSe ribbons after exposure to Se for 10 minutes at 330°C and 400°C, respectively. At both temperatures, the ribbons remain largely intact. Fig. 4 (d)-(f) and Figs. S4-S6 demonstrate that the surface morphology of the ribbons changes upon exposure to selenium compared to the initial GeSe surface, and that the final morphology is temperature dependent. At the lower temperature, we observe the development of a continuous shell that is ~80 nm thick and consists of amorphous $GeSe_2$ (a-$GeSe_2$) (Fig. S4). Raman linescans across the (a-$GeSe_2$)-GeSe heterostructures (Fig. S7) confirm the coexistence of the GeSe and a-$GeSe_2$ Raman modes uniformly across the heterostructure. At the higher temperature, Raman linescans across the $GeSe_2$-GeSe heterostructures (Fig. S8) show the characteristic Raman modes of GeSe together with a peak at 210 cm^{-1}, which corresponds to the most intense peak in monoclinic $GeSe_2$ as observed in the Raman spectra of pure single crystalline monoclinic $GeSe_2$ ribbons (Fig. S1). The peak at 210 cm^{-1} is a fingerprint of the crystalline $GeSe_2$. Its intensity is significantly lower than the GeSe peaks since the converted surface $GeSe_2$ layer is much thinner than the remaining GeSe core of the ribbons. The peak at 210 cm^{-1} is present along the entire linescan suggesting that the surface transformation from GeSe to $GeSe_2$ is uniform across the surface of the heterostructure. Electron diffraction on $GeSe_2$-GeSe heterostructures formed by selenization of GeSe ribbons at higher temperatures shows the appearance of additional spots, confirming the formation of a crystalline phase at the surface (Fig. 4 (e)). High-resolution TEM at this stage shows the lattice of single-crystalline GeSe accompanied by a uniform stripe moiré pattern, whose superlattice repeat distance is consistently ~2.5 nm (Fig. S5). The uniformity of the superstructure suggests a

well-defined, selenium exposure-induced modification to the GeSe layers. The additional diffraction spots are consistent with the [001] oriented monoclinic (*i.e.*, layered) β-$GeSe_2$. After selenization, the moiré fringes uniformly cover the entire GeSe ribbons, indicating a complete transformation of the surface layers from GeSe to $GeSe_2$, while preserving a GeSe core (consistent with the results of Raman spectroscopy and mapping, shown in Fig. S8). The stripe orientation varies somewhat across the ribbons, suggesting that the transformation starts simultaneously at different positions and progresses until the entire surface is converted.

In addition to converting the near-surface layers to $GeSe_2$, selenization also affects the open edges of the ribbons. At 400°C, there is clearly some loss of GeSe from the edges that leads to a thinning of the edge region compared to the center of the ribbons (Fig. S6). High-resolution TEM images obtained near the edge show ordered lattice fringes without any moiré structure, indicative of the presence of just one crystalline phase, different from the starting GeSe (Fig. S5 (b)), which can be identified from the FFT as [001] oriented $GeSe_2$ (Fig. S6 (c)). Fig. S9 summarizes the combined effects of selenization at high temperature: *(i)* Reaction of the topmost GeSe layers to parallel layered $GeSe_2$; and *(ii)* simultaneous thinning by GeSe loss and reaction to $GeSe_2$ at the ribbon edges.

To identify effects caused by the transformation of GeSe ribbons into GeSe-$GeSe_2$ heterostructures, we probed the optoelectronic properties before and after selenization using cathodoluminescence spectroscopy excited by the focused electron beam in HAADF-STEM (STEM-CL). STEM-CL spectra of the original GeSe ribbons and of ribbons of the same thickness following Se exposure (*i.e.*, terminated by $GeSe_2$) were measured under identical conditions (Fig. 4 (g)). The light emission of the as-grown GeSe ribbon (blue curve) consists of a sharp peak at 1.37 eV photon energy, consistent with GeSe band-edge luminescence.[2,18] The

GeSe-$GeSe_2$ heterostructure after selenization show bright luminescence with uniform intensity as seen in panchromatic CL maps (Fig. S10). The luminescence of the GeSe-$GeSe_2$ heterostructure is significantly enhanced, with a ~1.7-fold increase in intensity of the band-edge peak. This finding shows that $GeSe_2$ termination is effective in suppressing nonradiative surface recombination in GeSe, which is responsible for its low luminescence intensity at room temperature.[41] We note the presence of a higher-energy emission at ~2 eV photon energy for both as-grown and selenized GeSe ribbons (Fig. 4 (g)). Such transitions at energies well above the fundamental bandgap are frequently observed in CL,[42] but their precise origin tends to be difficult to ascertain. Finally, since the $GeSe_2$ termination is ultrathin, it does not give rise to CL peaks with sufficient intensity to be detected or interpreted.[31]

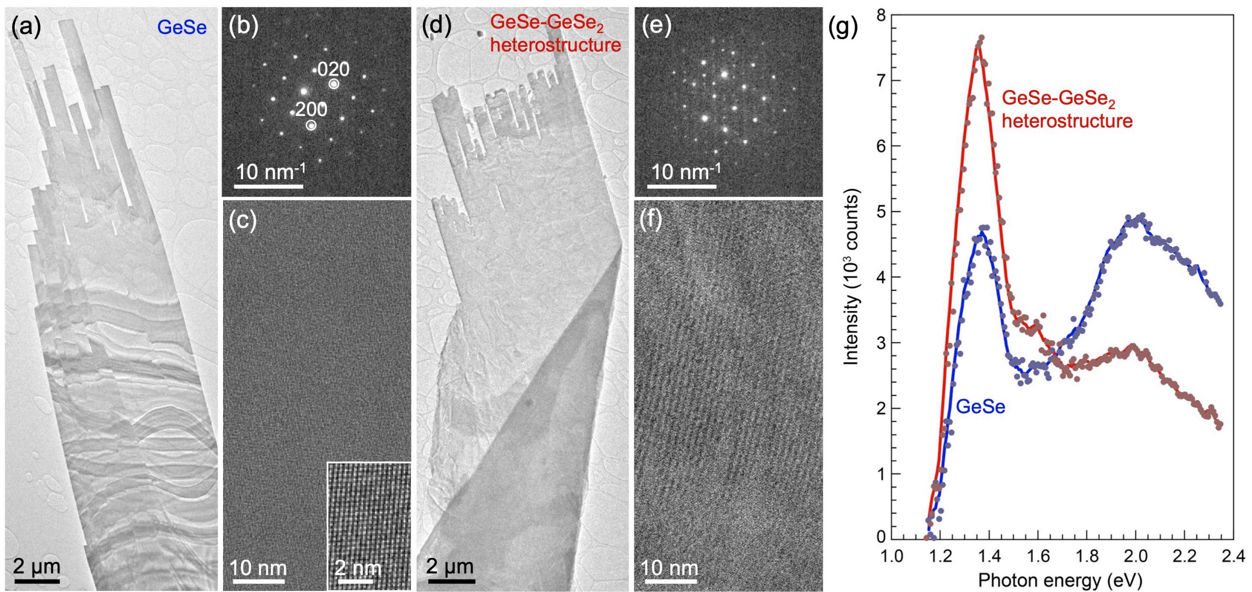

Figure 4. Morphology and luminescence of individual GeSe nanoribbons before and after selenization at 400°C. (a) TEM image of a starting GeSe nanoribbon grown by a VLS process involving GeSe vapor transport over Au catalyst particles on Si(100) (substrate temperature: 400°C). **(b)** Electron diffraction pattern of the GeSe ribbon (zone axis (ZA): [001]). **(c)** High-resolution TEM image of the uniform GeSe ribbon. Inset: Higher magnification image of the lattice fringes of the GeSe basal plane. **(d)** GeSe nanoribbon after exposure to selenium at 400°C. **(e)** Electron diffraction pattern, and **(f)** high-resolution TEM image of part of the selenized GeSe ribbon showing the superposition of GeSe spots ([001] zone axis) and $GeSe_2$ spots ([001] zone axis) and the appearance of stripe moiré fringes with a periodicity of ~2.5 nm. **(g)** STEM cathodoluminescence (STEM-CL) spectra of an as-grown GeSe ribbon (blue spectrum) and of a GeSe ribbon of equal thickness following reaction with selenium (red spectrum).

CONCLUSIONS

We demonstrated the phase-controlled vapor-liquid-solid synthesis of single-crystalline layered GeSe and $GeSe_2$ ribbons by vapor transport of GeSe and of GeSe and Se precursors, respectively. A detailed TEM investigation of the $GeSe_2$ ribbons shows that the growth proceeds *via* a combination of Au-catalyzed expansion in length and edge attachment that results in tapered ribbons that often decrease in thickness at one of the edges. In contrast to ribbons of other 2D layered materials, we observe that additional non-specific growth by direct precursor adsorption from the vapor phase can initiate on the surface of the $GeSe_2$ ribbons after a certain length, correlated with an extended exposure to the precursors. This growth is observed to start at the stepped edge of the ribbons, and it involves a well-defined crystallographic orientation that is different from the underlying $GeSe_2$. While the ribbons themselves remain 20-25 nm thin throughout, the additional non-specific growth can result in a significant local thickening. While our growth processes employed vapor transport at near-ambient pressures, synthesis in other environments (*e.g.*, ultrahigh vacuum) can be envisioned, albeit likely using different precursors, for example from gas sources. The focus of this work was on nanostructures obtained by metal catalyzed VLS growth, but modifications of our processes should allow the phase-selected growth of extended layers for wafer-scale applications.

Solid-state selenization of GeSe ribbons is shown to result in the conversion of the outermost layers and edges to $GeSe_2$, thus generating GeSe-$GeSe_2$ heterostructures. TEM imaging establishes that GeSe nanoribbons remain largely intact during vapor-phase reaction with Se at elevated temperatures and demonstrates the formation of $GeSe_2$ shells, amorphous at lower temperatures (330°C) and crystalline with $GeSe_2$ layers parallel to the layering of the underlying GeSe at higher temperatures (400°C). Cathodoluminescence spectroscopy on individual ribbons

establishes that the low-energy luminescence in both as-grown GeSe ribbons as well as GeSe-$GeSe_2$ heterostructures is dominated by the GeSe band-edge emission at 1.27 eV photon energy. The luminescence intensity of ribbons terminated by crystalline $GeSe_2$ is considerably enhanced compared to as-grown GeSe ribbons, indicating an effective surface passivation by wide-bandgap $GeSe_2$ that can be used to suppress non-radiative recombination in photovoltaics and other optoelectronic applications. This finding raises questions regarding the band offsets at the GeSe-$GeSe_2$ interface. To the best of our knowledge, the offsets and junction type (straddling gap, type I; or staggered gap, type II) have not been determined for this particular materials combination. The enhanced luminescence in $GeSe_2$-GeSe heterostructures compared with GeSe ribbons could be interpreted as a sign for a type I junction, but it may instead be explained *via* a passivation of gap states (*i.e.*, elimination of non-radiative recombination centers) by the thin $GeSe_2$ layer. As an immediate application, we foresee that the $GeSe_2$ termination obtained by reaction of GeSe with Se can be employed as a passivation layer to reduce radiative recombination at the interface of a p-type GeSe absorber and an n-type CdS window layer in efforts to enhance the efficiency of GeSe-based photovoltaic devices.[20] This and other applications are facilitated by the excellent ambient stability of both GeSe[20] and $GeSe_2$, evidenced by the absence of any detectable changes in our materials over time spans of several months.

MATERIALS AND METHODS

GeSe and $GeSe_2$ ribbons were synthesized in a pumped quartz tube reactor with two independently controlled temperature zones. The growth of GeSe ribbons used evaporation of a pure GeSe precursor (99.99%; ALB Materials), while $GeSe_2$ ribbons were obtained by co-evaporation of GeSe powder (99.99%; ALB Materials) and Se shot (1-6 mm, 99.999+%; Alfa

Aesar). The evaporation zone containing a quartz boat with the GeSe powder was heated to 500°C, while the zone containing the substrate was heated to growth temperatures of 280-340°C (GeSe ribbons) and 400°C ($GeSe_2$ ribbons), respectively. For $GeSe_2$ growth, a separate quartz boat containing Se was placed 5 cm outward from the GeSe boat in the evaporation zone. Melting of the Se shows that the temperature of the Se boat was above 220°C during growth. The configuration of the reactor for VLS synthesis of GeSe and $GeSe_2$ nanoribbons is shown in Fig. S11 (a), (b). Si(100) covered with nominally 2-5 nm Au films, deposited by sputtering at room temperature and dewetted at the growth temperature,[43] was used as substrate. During growth, a carrier gas (Ar, 99.9999%, Matheson) flow was maintained at 60 standard cubic centimeters per minute (sccm) and a pressure of 20 mTorr. Growth was typically performed for 5 minutes after which the reactor cooled naturally to room temperature.

Selenization experiments were carried out in a two-zone quartz reactor on as-grown GeSe ribbons, obtained by GeSe vapor transport onto Au/Si(100) (as described above) at a substrate temperature of 400°C.[2] Selenium shot (99.999+%, Alfa Aesar) was loaded into a quartz boat and placed in the center of the evaporation zone, which was heated to temperatures between 200°C and 350°C. During the selenization reaction, the GeSe ribbons were heated to temperatures between 330°C and 400°C. The configuration of the reactor for selenization of GeSe nanoribbons is shown in Fig. S11 (c). To ensure constant conditions during the reaction, the two zones were ramped so as to reach the chosen temperature setpoints at the same time. The Se exposure time was typically 10 minutes, after which the reactor cooled naturally to room temperature.

Optical microscopy and micro-Raman spectroscopy/mapping were performed in air in an optical/Raman microscope (Horiba Xplora plus). Optical imaging employed a 100× objective

and image stitching to cover large sample areas. Raman spectroscopy was performed with a 100× objective at 532 nm excitation wavelength and 16.8 μW laser power. Raman spectra and linescans were measured using a 300 μm pinhole at ~0.5 μm spatial resolution.

Structure, morphology, and optoelectronic properties of the ribbons were investigated by (scanning) transmission electron microscopy ((S)TEM) and electron diffraction in an FEI Talos F200X microscope operated at 200 kV, on ensembles of nanoribbons dry-transferred onto lacey carbon grids. Cathodoluminescence measurements were performed in HAADF-STEM (STEM-CL) using a Gatan Vulcan CL holder at room temperature. The system is configured to analyze and detect light at visible and near-infrared wavelengths between ~400-1000 nm. The incident electron beam current for CL measurements was typically 400 pA at an integration time of 10 s per spectrum. CL spectra were obtained on as-grown and selenized GeSe ribbons with identical thickness, determined by measuring the attenuation of the electron beam current in HAADF-STEM.[44]

Acknowledgements. This work was supported by the National Science Foundation, Division of Materials Research, Solid State and Materials Chemistry Program under Grant No. DMR-1904843.

Competing Interests. The authors declare no competing interests.

Supporting Information: Supporting Figures: TEM images of $GeSe_2$ ribbons; TEM images of a-$GeSe_2$/GeSe heterostructures; stripe moiré pattern of crystalline $GeSe_2$/GeSe heterostructures; transformation of the near-edge region during selenization at 400°C; optical microscopy images of the ribbons and heterostructures; Raman spectra and linescans of the $GeSe_2$ ribbons and $GeSe_2$/GeSe heterostructures; panchromatic CL map of a $GeSe_2$/GeSe heterostructure; schematic showing the effects of reaction of GeSe ribbons with Se at high temperatures; reactor configuration for synthesis of GeSe and $GeSe_2$ nanoribbons, as well as solid-state selenization (PDF).

REFERENCES

1. Okazaki, A. The Crystal Structure of Germanium Selenide GeSe. *J. Phys. Soc. Japan* **1958**, *13*, 1151-1155.
2. Sutter, E.; French, J. S.; Sutter, P. Free-standing large, ultrathin germanium selenide van der Waals ribbons by combined vapor–liquid–solid growth and edge attachment. *Nanoscale* **2022**, *14*, 6195-6201.
3. Wiedemeier, H.; Schnering, H. G. V. Refinement of the Structures of GeS, GeSe, SnS and SnSe. *Z. Kristallogr.* **1978**, *148*, 295-303.
4. Sutter, E.; Zhang, B.; Sun, M.; Sutter, P. Few-Layer to Multilayer Germanium(II) Sulfide: Synthesis, Structure, Stability, and Optoelectronics. *ACS Nano* **2019**, *13*, 9352-9362.
5. Sutter, P.; Komsa, H. P.; Lu, H.; Gruverman, A.; Sutter, E. Few-layer tin sulfide (SnS): Controlled synthesis, thickness dependent vibrational properties, and ferroelectricity. *Nano Today* **2021**, *37*, 101082.
6. Hazen, R. M.; Finger, L. W. The crystal structures and compressibilities of layer minerals at high pressure; I, SnS< 2), berndtite. *Am. Min.* **1978**, *63*, 289-292.
7. Dittmar, G.; Schafer, H. Die Kristallstruktur von Germaniumdiselenid. *Acta Crystallogr. B* **1976**, *32*, 2726-2728.
8. Mutlu, Z.; Wu, R. J.; Wickramaratne, D.; Shahrezaei, S.; Liu, C.; Temiz, S.; Patalano, A.; Ozkan, M.; Lake, R. K.; Mkhoyan, K. A.; Ozkan, C. S. Phase Engineering of 2D Tin Sulfides. *Small* **2016**, *12*, 2998-3004.
9. Sutter, E.; Huang, Y.; Komsa, H. P.; Ghorbani-Asl, M.; Krasheninnikov, A. V.; Sutter, P. Electron-Beam Induced Transformations of Layered Tin Dichalcogenides. *Nano Lett.* **2016**, *16*, 4410-4416.
10. Sutter, P.; Komsa, H.-P.; Krasheninnikov, A. V.; Huang, Y.; Sutter, E. Luminescence of defects in the structural transformation of layered tin dichalcogenides. *Appl. Phys. Lett.* **2017**, *111*, 262102.
11. Sutter, P.; Ibragimova, R.; Komsa, H.-P.; Parkinson, B. A.; Sutter, E. Self-organized twist-heterostructures via aligned van der Waals epitaxy and solid-state transformations. *Nat. Commun.* **2019**, *10*, 5528.
12. Sutter, P.; Wang, J.; Sutter, E. Wrap-Around Core–Shell Heterostructures of Layered Crystals. *Adv. Mater.* **2019**, *31*, 1902166.
13. Wang, X.; Li, Y.; Huang, L.; Jiang, X.-W.; Jiang, L.; Dong, H.; Wei, Z.; Li, J.; Hu, W. Short-Wave Near-Infrared Linear Dichroism of Two-Dimensional Germanium Selenide. *J. Am. Chem. Soc.* **2017**, *139*, 14976-14982.
14. Liu, J.; Zhou, Y.; Lin, Y.; Li, M.; Cai, H.; Liang, Y.; Liu, M.; Huang, Z.; Lai, F.; Huang, F.; Zheng, W. Anisotropic Photoresponse of the Ultrathin GeSe Nanoplates Grown by Rapid Physical Vapor Deposition. *ACS Appl. Mater. Interf.* **2019**, *11*, 4123-4130.
15. Mukherjee, B.; Cai, Y.; Tan, H. R.; Feng, Y. P.; Tok, E. S.; Sow, C. H. NIR Schottky Photodetectors Based on Individual Single-Crystalline GeSe Nanosheet. *ACS Appl. Mater. Interf.* **2013**, *5*, 9594-9604.

16. Zhou, X.; Hu, X.; Jin, B.; Yu, J.; Liu, K.; Li, H.; Zhai, T. Highly Anisotropic GeSe Nanosheets for Phototransistors with Ultrahigh Photoresponsivity. *Adv. Sci.* **2018**, *5*, 1800478.
17. Guan, S.; Liu, C.; Lu, Y.; Yao, Y.; Yang, S. A. Tunable ferroelectricity and anisotropic electric transport in monolayer β-GeSe. *Phys. Rev. B* **2018**, *97*, 144104.
18. Murgatroyd, P. A. E.; Smiles, M. J.; Savory, C. N.; Shalvey, T. P.; Swallow, J. E. N.; Fleck, N.; Robertson, C. M.; Jäckel, F.; Alaria, J.; Major, J. D.; Scanlon, D. O.; Veal, T. D. GeSe: Optical Spectroscopy and Theoretical Study of a van der Waals Solar Absorber. *Chem. Mater.* **2020**, *32*, 3245-3253.
19. Zi, W.; Mu, F.; Lu, X.; Cao, Y.; Xie, Y.; Fang, L.; Cheng, N.; Zhao, Z.; Xiao, Z. Post-annealing treatment of a-GeSe thin films for photovoltaic application. *Sol. Energy* **2020**, *199*, 837-843.
20. Liu, S.-C.; Dai, C.-M.; Min, Y.; Hou, Y.; Proppe, A. H.; Zhou, Y.; Chen, C.; Chen, S.; Tang, J.; Xue, D.-J.; Sargent, E. H.; Hu, J.-S. An antibonding valence band maximum enables defect-tolerant and stable GeSe photovoltaics. *Nat. Commun.* **2021**, *12*, 670.
21. Zhou, X.; Hu, X.; Zhou, S.; Zhang, Q.; Li, H.; Zhai, T. Ultrathin 2D $GeSe_2$ Rhombic Flakes with High Anisotropy Realized by Van der Waals Epitaxy. *Adv. Funct. Mater.* **2017**, *27*, 1703858.
22. Yumigeta, K.; Brayfield, C.; Cai, H.; Hajra, D.; Blei, M.; Yang, S.; Shen, Y.; Tongay, S. The synthesis of competing phase GeSe and $GeSe_2$ 2D layered materials. *RSC Adv.* **2020**, *10*, 38227-38232.
23. Zhang, L.; Yu, H.; Yang, Y.; Yang, K.; Dong, Y.; Huang, S.; Dai, N.; Zhu, D.-M. Synthesis of $GeSe_2$ Nanobelts Using Thermal Evaporation and Their Photoelectrical Properties. *J. Nanomater.* **2014**, *2014*, 310716.
24. Mukherjee, B.; Hu, Z.; Zheng, M.; Cai, Y.; Feng, Y. P.; Tok, E. S.; Sow, C. H. Stepped-surfaced $GeSe_2$ nanobelts with high-gain photoconductivity. *J. Mat. Chem.* **2012**, *22*, 24882-24888.
25. Mukherjee, B.; Murali, G.; Lim, S. X.; Zheng, M.; Tok, E. S.; Sow, C. H. Direct laser micropatterning of $GeSe_2$ nanostructures film with controlled optoelectrical properties. *RSC Adv.* **2014**, *4*, 10013-10021.
26. Mukherjee, B.; Tok, E. S.; Sow, C. H. Photocurrent characteristics of individual $GeSe_2$ nanobelt with Schottky effects. *J. Appl. Phys.* **2013**, *114*, 134302.
27. Yang, Y.; Wang, X.; Liu, S.-C.; Li, Z.; Sun, Z.; Hu, C.; Xue, D.-J.; Zhang, G.; Hu, J.-S. Weak Interlayer Interaction in 2D Anisotropic $GeSe_2$. *Adv. Sci.* **2019**, *6*, 1801810.
28. Yan, Y.; Xiong, W.; Li, S.; Zhao, K.; Wang, X.; Su, J.; Song, X.; Li, X.; Zhang, S.; Yang, H.; Liu, X.; Jiang, L.; Zhai, T.; Xia, C.; Li, J.; Wei, Z. Direct Wide Bandgap 2D $GeSe_2$ Monolayer toward Anisotropic UV Photodetection. *Adv. Opt. Mater.* **2019**, *7*, 1900622.
29. Yang, Y.; Liu, S.-C.; Yang, W.; Li, Z.; Wang, Y.; Wang, X.; Zhang, S.; Zhang, Y.; Long, M.; Zhang, G.; Xue, D.-J.; Hu, J.-S.; Wan, L.-J. Air-Stable In-Plane Anisotropic $GeSe_2$ for Highly Polarization-Sensitive Photodetection in Short Wave Region. *J. Am. Chem. Soc.* **2018**, *140*, 4150-4156.

30. Gao, W.; Zhou, G.; Li, J.; Chen, T.; Li, B.; Xiao, X.; Li, Y.; Huang, K.; Xiao, S.; Hao, G. Controllable epitaxial growth of $GeSe_2$ nanostructures and nonlinear optical properties. *Nanotechnol.* **2021**, *32*, 465704.
31. Sutter, P.; French, J. S.; Khosravi Khorashad, L.; Argyropoulos, C.; Sutter, E. Optoelectronics and Nanophotonics of Vapor–Liquid–Solid Grown GaSe van der Waals Nanoribbons. *Nano Lett.* **2021**, *21*, 4335-4342.
32. Sutter, E.; French, J. S.; Sutter, S.; Idrobo, J. C.; Sutter, P. Vapor–Liquid–Solid Growth and Optoelectronics of Gallium Sulfide van der Waals Nanowires. *ACS Nano* **2020**, *14*, 6117-6126.
33. Sutter, P.; Wimer, S.; Sutter, E. Chiral twisted van der Waals nanowires. *Nature* **2019**, *570*, 354-357.
34. Sutter, P.; Idrobo, J.-C.; Sutter, E. Van der Waals Nanowires with Continuously Variable Interlayer Twist and Twist Homojunctions. *Adv. Funct. Mater.* **2021**, *31*, 2006412.
35. Bernaerts, D.; Amelinckx, S.; Van Tendeloo, G.; Van Landuyt, J. Microstructure and formation mechanism of cylindrical and conical scrolls of the misfit layer compounds $PbNb_nS_{2n+1}$. *J. Cryst. Growth* **1997**, *172*, 433-439.
36. Radovsky, G.; Popovitz-Biro, R.; Tenne, R. Study of Tubular Structures of the Misfit Layered Compound SnS_2/SnS. *Chem. Mater.* **2012**, *24*, 3004-3015.
37. Sutter, E.; French, J. S.; Balgarkashi, A.; Tappy, N.; Fontcuberta i Morral, A.; Idrobo, J. C.; Sutter, P. Single-Crystalline γ-Ga_2S_3 Nanotubes via Epitaxial Conversion of GaAs Nanowires. *Nano Lett.* **2019**, *19*, 8903-8910.
38. Keiser, C.; Sutter, P.; Sutter, E. Formation of Ge–GeS core–shell nanostructures via solid-state sulfurization of Ge nanowires. *CrystEngComm* **2018**, *20*, 2193-2200.
39. Chen, H.; Keiser, C.; Du, S.; Gao, H.-J.; Sutter, P.; Sutter, E. Termination of Ge surfaces with ultrathin GeS and GeS_2 layers via solid-state sulfurization. *Phys. Chem. Chem. Phys.* **2017**, *19*, 32473-32480.
40. Yoon, S. M.; Song, H. J.; Choi, H. C. p-Type Semiconducting GeSe Combs by a Vaporization–Condensation–Recrystallization (VCR) Process. *Adv. Mater.* **2010**, *22*, 2164-2167.
41. Li, X.; Zhang, X.; Lv, X.; Pang, J.; Lei, L.; Liu, Y.; Peng, Y.; Xiang, G. Synthesis and photoluminescence of high density GeSe triangular nanoplate arrays on Si substrates. *Nanotechnol.* **2020**, *31*, 285702.
42. Sutter, P.; Argyropoulos, C.; Sutter, E. Germanium Sulfide Nano-Optics Probed by STEM-Cathodoluminescence Spectroscopy. *Nano Lett.* **2018**, *18*, 4576-4583.
43. Sutter, E.; Ozturk, B.; Sutter, P. Selective growth of Ge nanowires by low-temperature thermal evaporation. *Nanotechnol.* **2008**, *19*, 435607-435613.
44. Sutter, E.; French, J. S.; Komsa, H.-P.; Sutter, P. 1D Germanium Sulfide van der Waals Bicrystals by Vapor–Liquid–Solid Growth. *ACS Nano* **2022**, *16*, 3735-3743.

TOC Graphic